




Article

Performance of Carbide Alloy Compounds in Carbon Doped MoNbTaW

Congyan Zhang ¹, Uttam Bhandari ^{1,2} , Jialin Lei ¹, Congyuan Zeng ², Shengmin Guo ² , Hyunjoo Choi ³, Seungjin Nam ³, Jinyuan Yan ⁴, Shizhong Yang ¹  and Feng Gao ^{5,*}

¹ Department of Computer Science, Southern University and A&M College, Baton Rouge, LA 70813, USA; congyan_zhang@subr.edu (C.Z.); uttam.bhandari@sus.edu (U.B.); jialin.lei@sus.edu (J.L.); shizhong_yang@subr.edu (S.Y.)

² Department of Mechanical and Industrial Engineering, Louisiana State University, Baton Rouge, LA 70803, USA; czeng8@lsu.edu (C.Z.); sguo2@lsu.edu (S.G.)

³ School of Advanced Materials Engineering, Kookmin University, Seoul 02707, Korea; hyunjoo@kookmin.ac.kr (H.C.); nsj81@kookmin.ac.kr (S.N.)

⁴ Lawrence Berkeley National Laboratory, Berkeley, CA 94720, USA; jyan@lbl.gov

⁵ Department of Physics, Southern University and A&M College, Baton Rouge, LA 70813, USA

* Correspondence: feng.gao@sus.edu; Tel.: +225-771-2327

Abstract: In this work, the performance of the carbon doped compositionally complex alloy (CCA) MoNbTaW was studied under ambient and high pressure and high temperature conditions. TaC and NbC carbides were formed when a large concentration of carbon was introduced while synthesizing the MoNbTaW alloy. Both FCC carbides and BCC CCA phases were detected in the sample compound at room temperature, in which the BCC phase was believed to have only refractory elements MoNbTaW while FCC carbide came from TaC and NbC. Carbides in the carbon doped MoNbTaW alloy were very stable since no phase transition was obtained even under 3.1 GPa and 870 °C by employing the resistor-heating diamond anvil cell (DAC) synchrotron X-ray diffraction technique. Via in situ examination, this study confirms the stability of carbides and MoNbTaW in the carbon doped CCA even under high pressure and high temperature.

Keywords: high entropy alloy; synchrotron X-ray diffraction; diamond anvil cell; high pressure and high temperature property; calculation of phase diagram



Citation: Zhang, C.; Bhandari, U.; Lei, J.; Zeng, C.; Guo, S.; Choi, H.; Nam, S.; Yan, J.; Yang, S.; Gao, F. Performance of Carbide Alloy Compounds in Carbon Doped MoNbTaW. *Crystals* **2021**, *11*, 1073. <https://doi.org/10.3390/cryst11091073>

Academic Editor: Sergio Brutti

Received: 9 July 2021

Accepted: 31 August 2021

Published: 4 September 2021

Publisher's Note: MDPI stays neutral with regard to jurisdictional claims in published maps and institutional affiliations.



Copyright: © 2021 by the authors. Licensee MDPI, Basel, Switzerland. This article is an open access article distributed under the terms and conditions of the Creative Commons Attribution (CC BY) license (<https://creativecommons.org/licenses/by/4.0/>).

1. Introduction

High entropy alloy (HEA) has drawn increasing attention because a combination of different elements can build a simple microstructure which has promising properties [1–7]. HEAs are defined as alloys with at least four or more principal elements which have a concentration between 5% and 35 at%, where the properties of HEA may be tunable based on the elements contained. Being more broadly defined than traditional HEAs, compositionally complex alloys (CCAs) may have more than one phase in the microstructures, in which the secondary phase can be precipitate, ordered, disordered, or amorphous phase [8,9]. HEAs/CCAs were generally explored by changing one element in the existing alloy or by adding additional elements with the purpose of enhancing performance such as mechanical properties of alloys. For example, it was reported that an additional Al element in $Al_xCoCrCuFeNi$ promotes the transition of FCC to BCC structure. Meanwhile, the Al element was claimed to be the key factor influencing the microhardness [10].

It has been reported carbon (C) addition is another powerful method for inducing remarkable precipitation strengthening of CCAs [11–18]. For instance, 3.0 at% C doped in the alloy CoCrFeMnNi could lead to increased tensile yield strength from 371 MPa to 792 MPa [17] because of the existence of nano-carbides which showed excellent balanced strength and ductility in the alloy. Another example of the carbide-forming alloy is the $Mo_{0.5}NbHf_{0.5}ZrTi$ refractory HEA, whose compressive strength and plasticity were

increased due to the formation of MC carbides with $M = \text{Nb, Hf, Zr, and Ti}$ when the concentration of C was only 0.3 at% [18]. It is found from the previous experimental findings that the formation of carbide phase and solution strengthening are key factors for enhancing hardness, plasticity, yield strength, and tensile strength in HEAs [19–21]. Bai et al. add 2.5 at% of C to $\text{Fe}_{36}\text{Mn}_{36}\text{Ni}_9\text{Al}_{10}$ high entropy alloy which increased mechanical properties such as plasticity, yield strength and tensile strength. It is expected that the addition of C enhanced the plasticity of MoNbTaW alloy. The performance of C doped CCAs with low concentrations of C have been investigated under normal or high temperature [11–18]. However, the carbides–CCA alloy with high concentrations of carbon, especially the compounds under both high temperature and high pressure, have not yet been investigated.

In many fields, such as the propulsion systems in aircraft engines and rockets, the key technologies rely on systems that operate at elevated pressure and temperature. The service life of these systems is limited by some critical components which rely on the material that can resist mechanical loads at high temperature and high pressure. Therefore, researchers in this field aim to develop materials that can operate at higher temperature and high pressure. Synchrotron x-ray diffraction (XRD) coupled with resistor-heating or laser-heating diamond anvil cell (DAC) technique can provide microstructural information under high temperature and high pressure at the same time [22–27], which makes it possible to study performance of materials under both high temperature and high pressure. The high pressure can easily be generated through DAC by compressing small samples between two opposing diamond culets, while the high temperature can be generated by heating DAC through laser or resistor. Laser-heated DAC [23–25] has become an important tool, but the lack of temperature measurement accuracy is an ongoing problem [24]. On the other hand, an electrical heater with adjustable voltage and current out of the resistor heated DAC [27,28] makes it easier to precisely control and measure the temperature.

In this work, we explored the formation of carbides in MoNbTaW alloy with large concentration of C introduced during the synthesis of MoNbTaW. The performance of carbide–CCA alloy was investigated at a high pressure of ~3.1 GPa and a high temperature up to ~870 °C by using the resistor-heating DAC synchrotron XRD technique. Our study shows that carbides could be easily formed by doping large concentrations of carbon to the alloy, and the compounds are still stable even under the tested high temperature and high pressure.

2. Materials and Methods

CCA alloy powders were mechanically alloyed via high-energy ball-milling from the powder mixture of Nb (99.8%, ~44 μm , Alfa Aesar, Korea), Mo (99.99%, <150 μm , Sigma-Aldrich Ltd., Korea), Ta (99.98%, ~149 μm , Alfa Aesar, Korea), and W (99.9%, ~12 μm , Sigma-Aldrich Ltd., Korea) powders. Stainless steel balls with a diameter of 5 mm were used as milling media. The ball-to-powder mass ratio was 10:1. Moreover, 3 wt% stearic acid ($\text{CH}_3(\text{CH}_2)_{16}\text{COOH}$) as both process control agent and carbon dopant was added to avoid cold welding and agglomeration of powders while doping the CCA alloy. After placing the powder mixture, ball, and stearic acid into the water-circulated chamber, attrition milling was performed at 500 rpm for 96 h under an argon atmosphere. During the ball milling process, the carbon elements in the stearic acid were resolved in the Mo, Nb, Ta, and W mixture, which led to the large concentration of carbon in MoNbTaW CCA.

The performance of the obtained sample under high temperature and high pressure were investigated by using the resistor-heating DAC (BX90 Cell [26] (as shown in Figure 1a). The DAC synchrotron XRD data were collected at beamline 12.2.2 of the Advanced Light Source (ALS), Lawrence Berkeley National Laboratory (LBNL) [24]. As shown in Figure 1a, the cell has an annular space (24 mm outside diameter \times 14 mm inside diameter) inside the piston that allows the placement of a resistive heater. The cell also has U-shaped cuts in their cylinder part serving as wire inlets for thermocouples and electrode wires. The heater is an external tungsten heater [28] purchased from HPTLab. The basic framework of the

heater is a ring-shaped aluminum oxide holder with a tungsten wire coil inside. As the tungsten wire is subject to oxidation in air at elevated temperatures, the whole cell requires a protective can that keeps the DAC assembly in an inert gas mixture of argon + 2% H₂. The sample was loaded into a rhenium gasket with a sample chamber of 80 micron in diameter and held between the diamond anvils with 400 μm diameter culets. The scheme of the experiment setup is shown in Figure 1b. A gas membrane was used to control the pressure. The synchrotron XRD diffraction patterns were recorded by a MAR345 image plate at an energy of 25 keV with a $10 \times 10 \mu\text{m}^2$ spot size X-ray beam with the wavelength of 0.4959 Å. The standard material CeO₂ was used to calibrate the sample-detector distance and detector orientation. MgO powder was added as the medium for pressure transmission, and Pt powder was used to calibrate the pressure. The alloy sample mixed with MgO and Pt was firstly compressed to 3.1 GPa, then heated from room temperature to ~870 °C in 10 h while pressure kept at 3.1 GPa. In the end, the mixture was cooled down to room temperature in 2 h. The diffraction images were analyzed by Dioptas [29]. Scanning electron microscopy (SEM) with an energy dispersive spectroscopy (EDS) attachment was used for the microstructure observation and composition characterization. An accelerating voltage of 20 KV and a current of 4 nA were utilized. Clark Instrument, Model CM-802AT, Novi, MI, USA, was used to examine the hardness of the sintered bulk sample, the testing load of 1000 gf was used, and the dwell time was 15 s. To avoid the influence among indents, the interval between adjacent indents is over three times the diagonal of the indents.

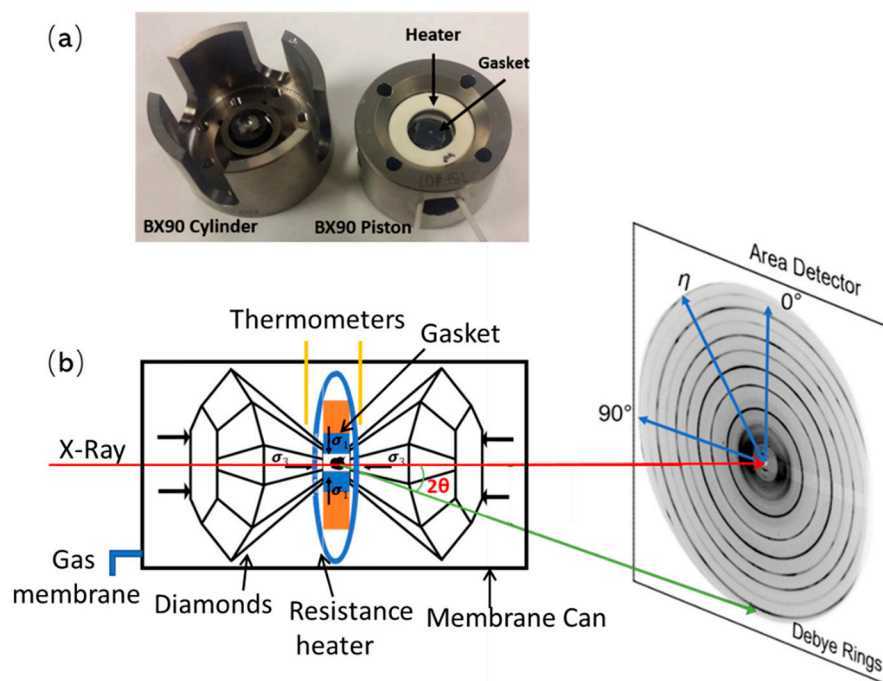


Figure 1. (a) The BX90 DAC. (b) The illustration of the radial synchrotron XRD experiment in a diamond anvil cell DAC with membrane (relevant details inside DAC are labeled in the Figure).

To investigate the formation of carbides in CCAs with various concentrations of C, phase diagrams predictions were performed through calculations using the CALPHAD software [30,31]. CALPHAD develops reliable, self-consistent thermodynamic databases that describe the Gibbs free energy of each individual phases in a system using semi-empirical equations. On the basis of the known descriptions of the constituent lower-order systems, the thermodynamic description for a higher order system can be obtained via an extrapolation method in the CALPHAD method. It represents that the Gibbs free energy of

multicomponent alloys can be extrapolated based on the binary A-B solution phase, which can be described as:

$$G_m^\phi = \sum_{i=A,B} x_i \cdot G_i^{\phi,0} + RT \sum_{i=A,B} x_i \ln x_i + x_A \cdot x_B \sum_{\nu} L_{\nu} \cdot (x_A - x_B)^{\nu} \quad (1)$$

where the first term of the equation represents the reference states with x_i , the mole fraction of a component, i , and $G_i^{\phi,0}$, and the Gibbs free energy of a pure component, i , with a ϕ structure. The second term is the ideal mixing term which is described by R , the gas constant, and temperature T . The last term is the excess Gibbs free energy of mixing with L_{ν} , the interaction coefficient, and ν , the power of the polynomial series. Equation (1) can be extrapolated into a multi-component system using geometric models, such as the Muggianu model [32]. For example, the ternary system with component of A-B-C, the Gibbs energy can be extrapolated from the binary ones:

$$G_{ternary} = A_{AB}G_{AB} + A_{AC}G_{AC} + A_{BC}G_{BC} + G_{ABC} \quad (2)$$

where A_{ij} is the coefficient which can be a function of composition used to extrapolate binary systems to ternary ones and G_{ij} is the Gibbs energy for binary system. Ternary and higher-order interaction parameters may be necessary to describe a multi-component solution phase. The related Thermo-Calc-2019 software was employed to predict the phase diagram of refractory alloys, in which the related Thermo-Calc's high entropy alloy database (TCHEA1) [33] was claimed to have good agreement with the experimental observations on the phase of refractory HEAs [34–38]. The CALPHAD calculation predicts the phase of MoNbTaW, which has only BCC phase under a temperature up to ~3000 K. The prediction is the same as the reported observations [5,39], which indicates the reliability of CALPHAD.

3. Results

The XRD patterns of ball milled carbon doped MoNbTaW (C-MoNbTaW) sample are shown in Figure 2 (black line). For comparison, the XRD of sintered bulk specimen synthesized by spark plasma sintering (SPS) is also shown in Figure 2 (see the red line in Figure 2). Both BCC and FCC (carbides) peaks were obtained in the sintered bulk specimen and ball milled sample. According to the Bragg's law, $\lambda = 2d_{hkl} \sin \theta_{hkl}$, for a cubic system, $d^2 = a^2 / (h^2 + k^2 + l^2)$, the lattice constant of FCC crystal calculated from the sintered bulk alloy is 3.072 Å, and BCC is 3.150 Å. The XRD peaks were broad in the ball milled powder because of the strain and crystallite size reduction, which led to the overlap of FCC and BCC peaks in the XRD. The scanning electron microscopy (SEM) images of carbon doped MoNbTaW particles are shown in Figure 3a,b. Clearly, the particles are irregular shaped with size of the obtained C-MoNbTaW ranging from 0.2 to 0.8 µm with an average value of 0.5 µm. The EDS analysis in Figure 3c confirmed that ~8.2 wt% of C was contained in the C-MoNbTaW sample. Figure 4 shows the microstructures, and the EDS mapping results of the bulk sintered sample. Pores are observed in the bulk sintered C-MoNbTaW sample, which is typical in samples made with powder metallurgy (indicated with white arrows in Figure 4a). There are mainly two areas in the sintered bulk sample, namely the bright area and the dark area. With the help of EDS mapping, the dark area is the enrichment of Nb and Ta elements, while the bright area indicates higher concentrations of W. Besides, Mo distributes uniformly throughout the material. Due to the limited amount of C, its signal is hardly observed. The average amount of C element on the sample surface was determined to be around 5.7 wt% in the bulk sintered sample. Compared with C content detected in the C-MoNbTaW particles, it is deduced that the higher concentration of C results from contaminants attached on the particle surfaces. In the meantime, the average Vickers hardness of bulk sintered C-MoNbTaW sample was tested at five different spots and average hardness was found to be 1668 HV with a standard deviation of 35 HV.

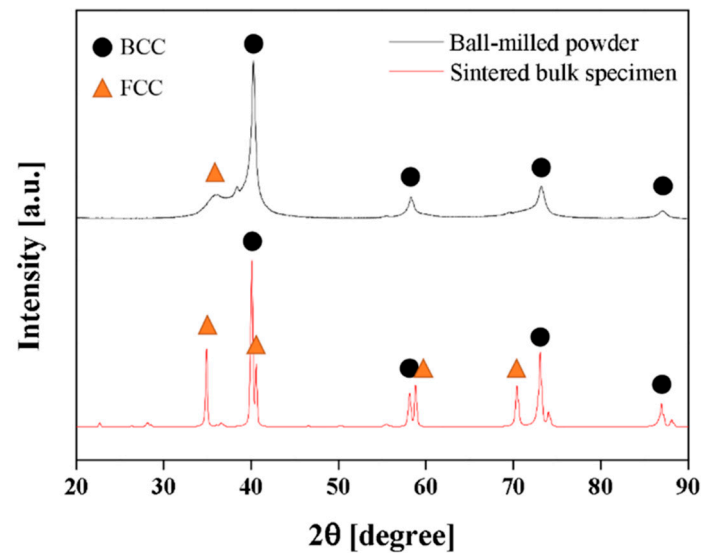


Figure 2. XRD pattern of carbon doped MoNbTaW ball milled powder (black) and sintered bulk specimen (red).

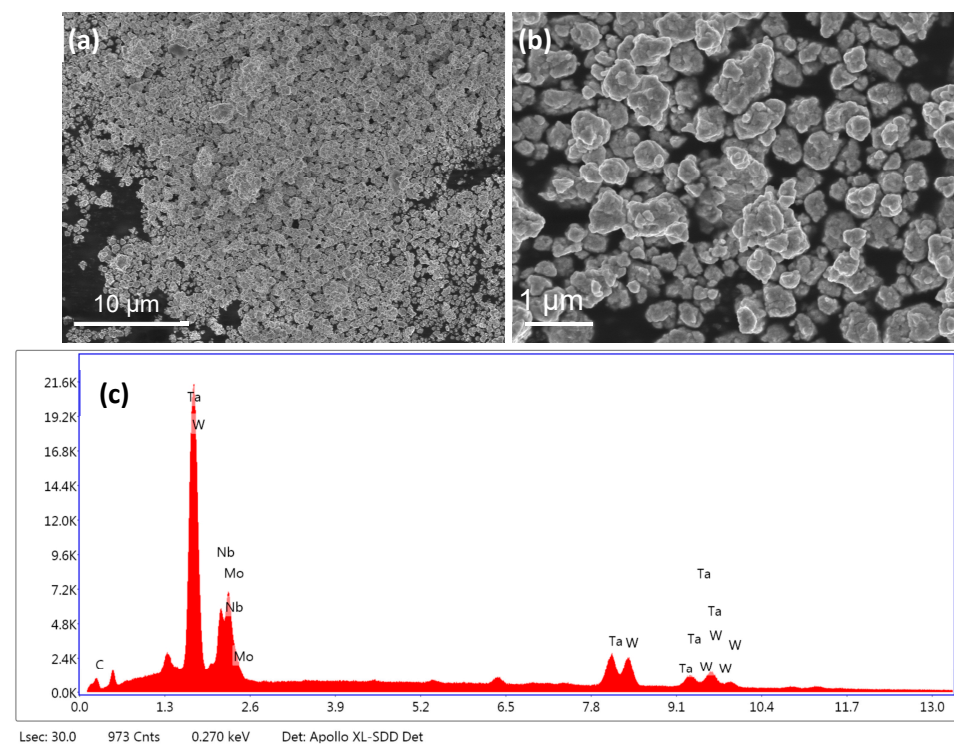


Figure 3. (a,b) Microstructure of C-MoNbTaW sample. (c) EDS analysis of carbon doped MoNbTaW.

In situ XRD patterns of the C-MoNbTaW/MgO/Pt mixtures obtained under various temperatures at 3.1 GPa are demonstrated in Figure 5. These XRD patterns are used to investigate the phase stability of C-MoNbTaW under high pressure and high temperature. The XRD peaks of MgO, Pt, and samples are marked by black, red, and blue dots, respectively. The major peaks include: MgO 111, 311, and 222 peaks, (the MgO 200 and 220 peaks are replaced by dash lines to guarantee a better view of sample peaks); Pt 111, 200, and 220 peaks; carbides (FCC) 111, 200, 220, 311, and 222 peaks; and MoNbTaW (BCC) 110, 200, and 211 peaks. As stated in Figure 2, the FCC 200 and BCC 110, FCC 220 and BCC 200, and FCC 311, 222, and BCC 211 are overlapped because of the close peak position, thus, only four main peaks of the sample can be clearly observed. Under 3.1 GPa and

room temperature, the sample is identified to have BCC and FCC phases by DAC XRD, indicating the phase stability of the sample under a pressure up to ~ 3.1 GPa. Furthermore, peaks neither appear nor disappear when temperature is increased from room temperature to 870 °C with the pressure kept at 3.1 GPa, indicating that there is no phase transition at high temperature of 870 °C and high pressure of 3.1 GPa.

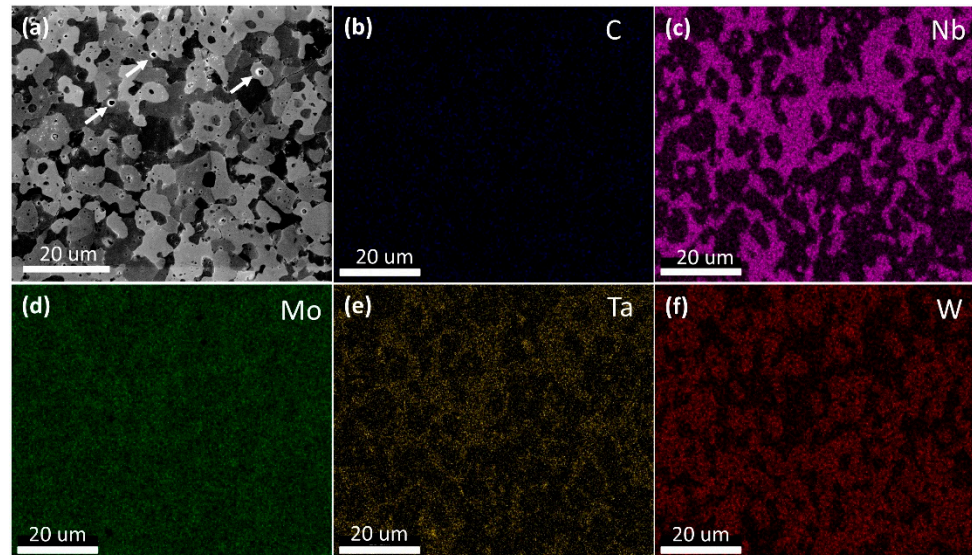


Figure 4. SEM image showing the microstructures of bulk sintered C-MoNbTaW sample (a), and the EDS mapping results indicating the composition distribution of elements (b) C, (c) Nb, (d) Mo, (e) Ta, and (f) W.

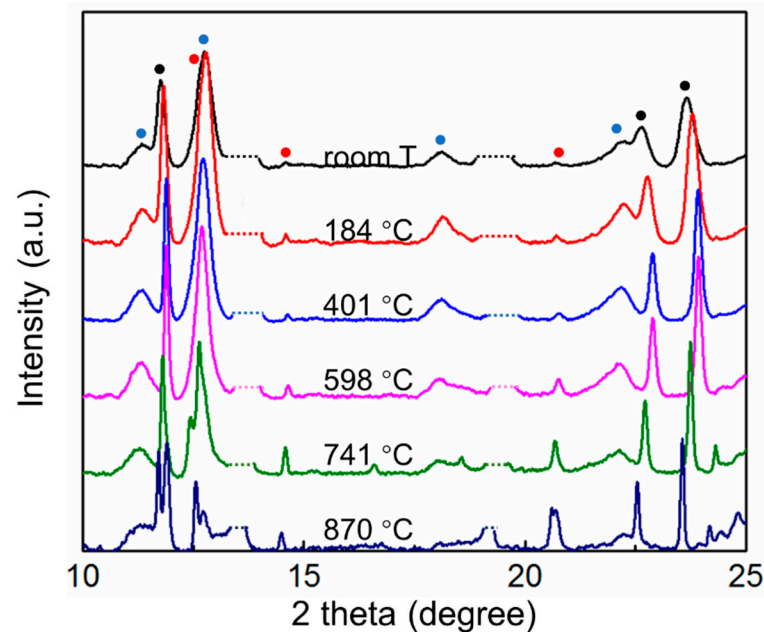


Figure 5. Synchrotron XRD patterns of C-MoNbTaW/MgO/Pt mixture with various temperatures; the pressure was kept at ~ 3.1 GPa.

4. Discussion

4.1. Carbides in the MoNbTaW Alloy

The BCC phase detected from XRD in Figure 2 belongs to the MoNbTaW alloy which was reported to have only BCC single phase even when the temperature reaches 1600 °C [5,39]. The FCC peaks were aligned through the open source XRD database Ma-

terial Projects, which shows that the FCC patterns belong to the carbides TaC/NbC. The intermetallic phase and carbides were formed by refractory metals interacting with the carbon in the stearic acid after long-time high-energy ball milling. A similar observation was reported when fabricating an AlFeMgTiZn alloy by ball milling, and the carbides were formed due to a small amount of stearic acid used during the process [40].

The values of chemical mixing enthalpy ΔH_{mix} (kJ/mol) of atomic pairs obtained from Miedema's model [41] and the electronegativity difference $\Delta\chi_r$ between C and the refractory elements are listed in Table 1. C-based binaries have a negative ΔH_{mix} which is much lower than that of the binary refractory compounds (ranging from -26 to 0 kJ/mol [41]). This indicates that carbides are easy to be formed when mixing C with refractory elements. Moreover, C-Ta and C-Nb pairs have larger $\Delta\chi_r$ than those of other C-refractory elements, which indicates a stronger attractive interaction between C and Ta/Nb. As a result, the binary compounds TaC/NbC were formed. Comparison of these two parameters shows that the most possible carbides obtained in the C-MoNbTaW alloy are TaC/NbC, which is consistent with the experimental observation.

Table 1. The Pauling scaled electronegativity difference $\Delta\chi_r$ and the chemical mixing enthalpy ΔH_{mix} (kJ/mol) of atomic pairs between C and the refractory elements.

Binary	Mo-C	Nb-C	Ta-C	W-C
ΔH_{mix}	-67	-102	-60	-42
$\Delta\chi_r$	0.39	0.95	1.05	0.19

The phase diagram of MoNbTaW and C-MoNbTaW under 3.0 GPa obtained by CALPHAD are plotted in Figure 6a,b. Very few amounts of HCP phase were obtained in C-MoNbTaW, as shown in Figure 6b. The composition analysis shows that the component in BCC phase include W, Ta, Mo, and Nb with the mole fraction of each element close to 0.25. The component in the HCP phase includes 0.54 mole fraction of Ta, 0.13 mole fraction of Nb, and 0.33 mole fraction of C, which indicates the formation of Ta-Nb-C carbides in MoNbTaW alloy.

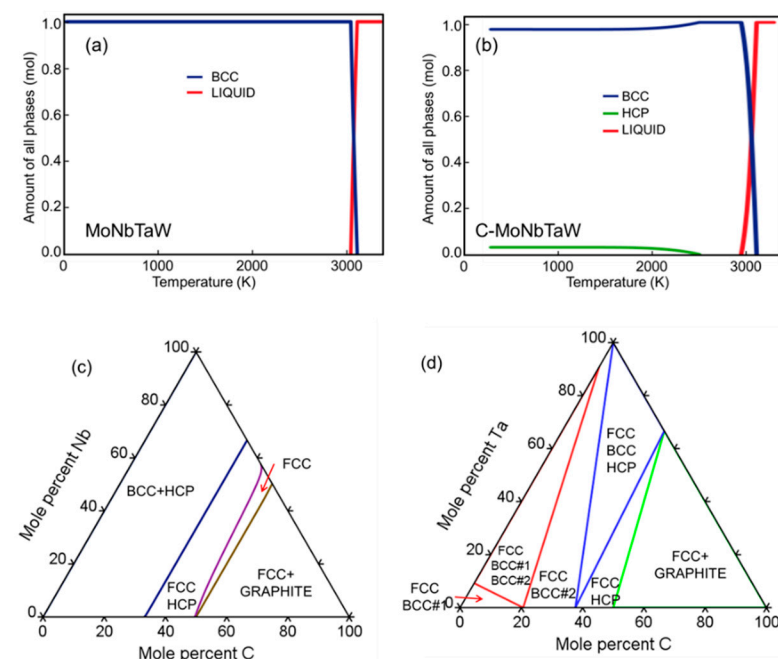


Figure 6. Phase diagram of (a) MoNbTaW, (b) C-MoNbTaW; phase diagram of TaNbC system with (c) mole percentage of Nb as the function of mole percentage of C under ambient temperature and pressure; (d) mole percentage of Ta as the function of mole percentage of C under ambient conditions.

According to the phase diagram, the $(\text{Ta/Nb})_2\text{C}$ carbides with the HCP phase were obtained. However, it is different from the experiment that $(\text{Ta/Nb})\text{C}$ carbides with FCC phase were obtained in the alloy. To explore the possible phase of the Nb-Ta-C system with various C concentrations under ambient conditions, its phase diagram was plotted in Figure 6c,d. As shown in the Figures, when the mole percentage of C is less than 50%, the phase of the Nb-Ta-C system would have a transition from BCC, HCP, to FCC with the increase in C mole percentage; the Nb-Ta-C system has only FCC and graphite phase when the mole percentage of C is more than 50%. It should be noticed that during the synthesis of C-MoNbTaW, metal powders were merged in the stearic acid. This can allow stearic acid to provide sufficient carbon elements to interact with refractory elements. On the other hand, the C element provided by stearic acid made it impossible to form the graphite phase during ball milling. In this case, even though the phase diagram predicted by CALPHAD indicates that the HCP phase could be formed in carbon doped MoNbTaW, the actual phase of carbides obtained in the ball milled alloy is FCC, considering the synthesis process.

4.2. C-MoNbTaW under High Pressure and High Temperature

It is clearly shown in Figure 5 that the full width at half maximum (FWHM) decreased with the increase in temperature up to 598 °C. The reason is that increasing temperature may enhance the order of the crystalline. On the other hand, the Pt 111 and the second peak of alloy (FCC 220 and BCC 200) are initially overlapped at the 2-theta value of ~12.5 degrees. The peak splitting is obtained when the temperature increases to 741 °C, making the Pt 111 and the FCC 220 and BCC 200 distinguishable due to the different change of crystalline size of Pt and C-MoNbTaW with the increase in temperature. While only a small amount of sample is detected when the temperature is 870 °C, the intensity of the alloy peaks is weak.

It is interesting that the diffraction peaks of both FCC and BCC peaks shift to smaller 2θ angles with temperature increased up to 741 °C, which indicates that the lattice expands based on the Bragg's law. The peaks shift to smaller 2θ angles with temperature increased in the range of 741 to 870 °C. The corresponding lattice as the function of temperature for BCC and FCC phase are shown in Figure 7. As shown in the Figure, the linear trend was obtained for lattice constant as a function of temperature as the temperature increased to 741 °C for both FCC and BCC lattice, which can be explained by the intrinsic nature of thermal expansion in the alloys due to the increasing atomic thermal vibration from their equilibrium positions [42]. The drop of lattice constant when the temperature increased from 741 to 870 °C is still under investigation.

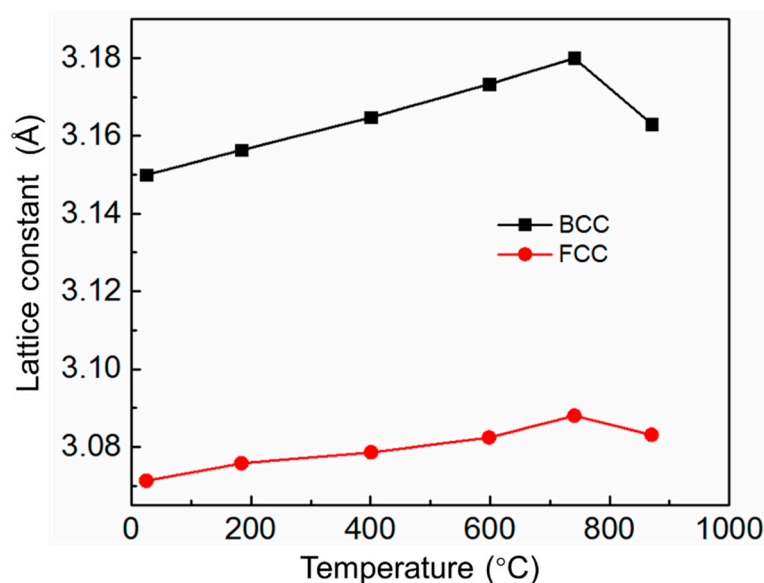


Figure 7. Lattice constant for BCC (black square) and FCC (carbide, red circle) as a function of temperature.

5. Conclusions

In this work, carbon doped MoNbTaW was synthesized by ball milling and studied under various temperatures at 3.1 GPa. Carbides TaC and NbC were formed by introducing acid to the mixture during the synthesis of MoNbTaW, which led to the coexistence of BCC (MoNbTaW) and carbide phase as obtained by XRD. The carbides are easy to obtain when a large concentration of carbon is mixed with refractory elements during ball milling according to the CALPHAD calculation. Both phases are very stable even when the temperature increased to 870 °C at 3.1 GPa. The mechanical properties of C-MoNbTaW are expected to be improved since carbides are the favorable phases in the form of hard constituents in metal matrix composites. The resistor-heating DAC used in this work performed high temperature and high pressure tests at the same time, which can be further applied to explore the performance of other alloys. Based on this in situ study, we demonstrated the carbides synthesizing method and the coexistence of highly stable phases in CCA at both high pressure and high temperature.

Author Contributions: C.Z. (Congyan Zhang): Conceptualization, methodology, data curation, original draft preparation. J.L.: Methodology, data curation. U.B.: Data curation. H.C., C.Z. (Congyuan Zeng), S.G., S.N.: sample preparation. J.Y.: Resources. F.G.: Conceptualization, original draft preparation. S.Y.: Conceptualization, Supervision. All authors: review and editing the manuscript. All authors have read and agreed to the published version of the manuscript.

Funding: This research was funded by NSF EPSCoR CIMM project under Award No. 1541079, CIMM LINK project, DOE/NNSA award No. DE-NA0003979, DoD support under contract No. W911NF1910005, NSF LAMDA and SEED funds: OIA-1946231 and LEQSF-EPS (2021)-LAMDA Seed-Track1B-04/LEQSF-EPS (2021)-LAMDASeed-Track1A-02, LEQSF-EPS (2020)-SURE-242/LEQSF-EPS (2020)-SURE-237. The Advanced Light Source is supported by the Director, Office of Science, Office of Basic Energy Sciences, of the U.S. Department of Energy, Grant No. DE-AC02-05CH11231. High performance computer simulation is supported by LONI allocation loni_mat_bio16.

Conflicts of Interest: The authors declare no conflict of interest.

References

- Koželj, P.; Vrtnik, S.; Jelen, A.; Jazbec, S.; Jagličič, Z.; Maiti, S.; Feuerbacher, M.; Steurer, W.; Dolinšek, J. Discovery of a Superconducting High-Entropy Alloy. *Phys. Rev. Lett.* **2014**, *113*, 107001. [\[CrossRef\]](#)
- Do, H.S.; Lee, B.J. Origin of radiation resistance in multi-principal element alloys. *Sci. Rep.* **2018**, *8*, 16015. [\[CrossRef\]](#) [\[PubMed\]](#)
- Terrani, K.A.; Ang, C.; Snead, L.L.; Katoh, Y. Irradiation stability and thermo-mechanical properties of NITE-SiC irradiated to 10 dpa. *J. Nucl. Mater.* **2018**, *499*, 242–247. [\[CrossRef\]](#)
- Miracle, D.B.; Senkov, O.N. A critical review of high entropy alloys and related concepts. *Acta Mater.* **2017**, *122*, 448–511. [\[CrossRef\]](#)
- Senkov, O.N.; Wilks, G.B.; Scott, J.M.; Miracle, D.B. Mechanical properties of Nb₂₅Mo₂₅Ta₂₅W₂₅ and V₂₀Nb₂₀Mo₂₀Ta₂₀W₂₀ refractory high entropy alloys. *Intermetallics* **2011**, *19*, 698–706. [\[CrossRef\]](#)
- Senkov, O.N.; Wilks, G.B.; Miracle, D.B.; Chuang, C.P.; Liaw, P.K. Refractory high-entropy alloys. *Intermetallics* **2010**, *18*, 1758–1765. [\[CrossRef\]](#)
- Kang, B.; Lee, J.; Ryu, H.J.; Hong, S.H. Ultra-high strength WNbMoTaV high-entropy alloys with fine grain structure fabricated by powder metallurgical process. *Mater. Sci. Eng. A* **2018**, *712*, 616–624. [\[CrossRef\]](#)
- Miracle, D.B.; Miller, J.D.; Senkov, O.N.; Woodward, C.; Uchic, M.D.; Tiley, J. Exploration and development of high entropy alloys for structural applications. *Entropy* **2014**, *16*, 494–525. [\[CrossRef\]](#)
- Gorsse, S.; Couzinié, J.P.; Miracle, D.B. From high-entropy alloys to complex concentrated alloys. *C. R. Phys.* **2018**, *19*, 721–736. [\[CrossRef\]](#)
- Ye, X.; Ma, M.; Liu, W.; Li, L.; Zhong, M.; Liu, Y.; Wu, Q. Synthesis and characterization of high-entropy alloy Al_xFeCoNiCuCr by laser cladding. *Adv. Mater. Sci. Eng.* **2011**, *2011*, 485942. [\[CrossRef\]](#)
- Klimova, M.V.; Semenyuk, A.O.; Shaysultanov, D.G.; Salishchev, G.A.; Zherebtsov, S.V.; Stepanov, N.D. Effect of carbon on cryogenic tensile behavior of CoCrFeMnNi-type high entropy alloys. *J. Alloys Compd.* **2019**, *811*, 152000. [\[CrossRef\]](#)
- Joo, S.H.; Kato, H.; Jang, M.J.; Moon, J.; Kim, E.B.; Hong, S.J.; Kim, H.S. Structure and properties of ultrafine-grained CoCrFeMnNi high-entropy alloys produced by mechanical alloying and spark plasma sintering. *J. Alloys Compd.* **2017**, *698*, 591–604. [\[CrossRef\]](#)
- Cheng, H.; Wang, H.Y.; Xie, Y.C.; Tang, Q.H.; Dai, P.Q. Controllable fabrication of a carbide-containing FeCoCrNiMn high-entropy alloy: Microstructure and mechanical properties. *Mater. Sci. Technol.* **2017**, *33*, 2032–2039. [\[CrossRef\]](#)
- Shun, T.-T.; Du, Y.-C. Age hardening of the Al_{0.3}CoCrFeNiC_{0.1} high entropy alloy. *J. Alloys Compd.* **2009**, *478*, 269–272. [\[CrossRef\]](#)

15. Velo, I.L.; Gotor, F.J.; Alcalá, M.D.; Real, C.; Córdoba, J.M. Fabrication and characterization of WC-HEA cemented carbide based on the CoCrFeNiMn high entropy alloy. *J. Alloys Compd.* **2018**, *746*, 1–8. [[CrossRef](#)]
16. Wu, Z.; Wang, C.; Zhang, Y.; Feng, X.; Gu, Y.; Li, Z.; Jiao, H.; Tan, X.; Xu, H. The AC Soft Magnetic Properties of FeCoNi_xCuAl (1.0 ≤ x ≤ 1.75) High-Entropy Alloys. *Mater. Res. Lett.* **2019**, *12*, 4222. [[CrossRef](#)] [[PubMed](#)]
17. Li, J.; Gao, B.; Wang, Y.; Chen, X.; Xin, Y.; Tang, S.; Liu, B.; Liu, Y.; Song, M. Microstructures and mechanical properties of nano carbides reinforced CoCrFeMnNi high entropy alloys. *J. Alloys Compd.* **2019**, *792*, 170–179. [[CrossRef](#)]
18. Guo, N.N.; Wang, L.; Luo, L.S.; Li, X.Z.; Chen, R.R.; Su, Y.Q.; Guo, J.J.; Fu, H.Z. Microstructure and mechanical properties of in-situ MC-carbide particulates-reinforced refractory high-entropy Mo_{0.5}NbHf_{0.5}ZrTi matrix alloy composite. *Intermetallics* **2016**, *69*, 74–77. [[CrossRef](#)]
19. Guo, L.; Ou, X.; Ni, S.; Liu, Y.; Song, M. Effects of carbon on the microstructures and mechanical properties of FeCoCrNiMn high entropy alloys. *Mater. Sci. Eng. A* **2019**, *746*, 356–362. [[CrossRef](#)]
20. Huang, T.; Jiang, L.; Zhang, C.; Jiang, H.; Lu, Y.; Li, T. Effect of carbon addition on the microstructure and mechanical properties of CoCrFeNi high entropy alloy. *Sci. China Technol. Sci.* **2018**, *61*, 117–123. [[CrossRef](#)]
21. Bai, L.; Wang, Y.; Yan, Y.; Li, X.; Lv, Y.; Chen, J. Effect of carbon on microstructure and mechanical properties of Fe₃₆Mn₃₆Ni₉Cr₉Al₁₀ high-entropy alloys. *Mater. Sci. Technol.* **2020**, *36*, 1851–1860. [[CrossRef](#)]
22. Yan, J.; Knight, J.; Kunz, M.; Vennila Raju, S.; Chen, B.; Gleason, A.E.; Godwal, B.K.; Geballe, Z.; Jeanloz, R.; Clark, S.M. The resistive-heating characterization of laser heating system and LaB₆ characterization of X-ray diffraction of beamline 12.2.2 at advanced light source. *J. Phys. Chem. Solids* **2010**, *71*, 1179–1182. [[CrossRef](#)]
23. Bassett, W.A. Diamond anvil cell, 50th birthday. *High Press. Res.* **2009**, *29*, 163–186. [[CrossRef](#)]
24. Kunz, M.; Yan, J.; Cornell, E.; Domning, E.E.; Yen, C.E.; Doran, A.; Beavers, C.M.; Treger, A.; Williams, Q.; MacDowell, A.A. Implementation and application of the peak scaling method for temperature measurement in the laser heated diamond anvil cell. *Rev. Sci. Instrum.* **2018**, *89*, 083903. [[CrossRef](#)]
25. Raju, S.V.; Zaug, J.M.; Chen, B.; Yan, J.; Knight, J.W.; Jeanloz, R.; Clark, S.M. Determination of the variation of the fluorescence line positions of ruby, strontium tetraborate, alexandrite, and samarium-doped yttrium aluminum garnet with pressure and temperature. *J. Appl. Phys.* **2011**, *110*, 023521. [[CrossRef](#)]
26. Kantor, I.; Prakapenka, V.; Kantor, A.; Dera, P.; Kurnosov, A.; Sinogeikin, S.; Dubrovinskaia, N.; Dubrovinsky, L. BX90: A new diamond anvil cell design for X-ray diffraction and optical measurements. *Rev. Sci. Instrum.* **2012**, *83*, 125102. [[CrossRef](#)]
27. Pasternak, S.; Aquilanti, G.; Pascarelli, S.; Poloni, R.; Canny, B.; Coulet, M.-V.; Zhang, L. A diamond anvil cell with resistive heating for high pressure and high temperature x-ray diffraction and absorption studies. *Rev. Sci. Instrum.* **2008**, *79*, 085103. [[CrossRef](#)] [[PubMed](#)]
28. Yan, J.; Doran, A.; MacDowell, A.A.; Kalkan, B. A tungsten external heater for BX90 diamond anvil cells with a range up to 1700 K. *Rev. Sci. Instrum.* **2021**, *92*, 013903. [[CrossRef](#)]
29. Prescher, C.; Prakapenka, V.B. DIOPTAS: A program for reduction of two-dimensional X-ray diffraction data and data exploration. *High Press. Res.* **2015**, *35*, 223–230. [[CrossRef](#)]
30. Chang, Y.A.; Chen, S.; Zhang, F.; Yan, X.; Xie, F.; Schmid-Fetzer, R.; Oates, W.A. Phase diagram calculation: Past, present and future. *Prog. Mater. Sci.* **2004**, *49*, 313–345. [[CrossRef](#)]
31. Kattner, U.R. The thermodynamic modeling of multicomponent phase equilibria. *JOM J. Miner. Met. Mater. Soc.* **1997**, *49*, 14. [[CrossRef](#)]
32. Muggianu, Y.M.; Gambino, M.; Bros, J.P. Enthalpies de formation des alliages liquides bismuth-étain-gallium à 723 K. Choix d’une représentation analytique des grandeurs d’excès intégrales et partielles de mélange. *J. Chim. Phys.* **1975**, *72*, 83–88. [[CrossRef](#)]
33. Andersson, J.O.; Helander, T.; Höglund, L.; Shi, P.; Sundman, B. Thermo-Calc & DICTRA, computational tools for materials science. *Calphad* **2002**, *26*, 273–312.
34. Gao, M.C.; Carney, C.S.; Doğan, Ö.N.; Jablonksi, P.D.; Hawk, J.A.; Alman, D.E. Design of refractory high-entropy alloys. *JOM* **2015**, *67*, 2653–2669. [[CrossRef](#)]
35. Yao, H.W.; Qiao, J.W.; Gao, M.C.; Hawk, J.A.; Ma, S.G.; Zhou, H.F.; Zhang, Y. NbTaV-(Ti,W) refractory high-entropy alloys: Experiments and modeling. *Mater. Sci. Eng. A* **2016**, *674*, 203–211. [[CrossRef](#)]
36. Yao, H.W.; Qiao, J.W.; Hawk, J.A.; Zhou, H.F.; Chen, M.W.; Gao, M.C. Mechanical properties of refractory high-entropy alloys: Experiments and modeling. *J. Alloys Compd.* **2017**, *696*, 1139–1150. [[CrossRef](#)]
37. Zhang, B.; Gao, M.C.; Zhang, Y.; Yang, S.; Guo, S.M. Senary refractory high entropy alloy MoNbTaTiVW. *Mater. Sci. Technol.* **2015**, *31*, 1207–1213. [[CrossRef](#)]
38. Han, Z.D.; Luan, H.W.; Liu, X.; Chen, N.; Li, X.Y.; Shao, Y.; Yao, K.F. Microstructures and mechanical properties of Ti_xNbMoTaW refractory high-entropy alloys. *Mater. Sci. Eng. A* **2018**, *712*, 380–385. [[CrossRef](#)]
39. Han, J.; Su, B.; Lu, J.; Meng, J.; Zhang, A.; Wu, Y. Preparation of MoNbTaW refractory high entropy alloy powders by pressureless spark plasma sintering: Crystal structure and phase evolution. *Intermetallics* **2020**, *123*, 106832. [[CrossRef](#)]
40. Hammond, V.H.; Atwater, M.A.; Darling, K.A.; Nguyen, H.Q.; Kecskes, L.J. Equal-channel angular extrusion of a low-density high-entropy alloy produced by high-energy cryogenic mechanical alloying. *JOM* **2014**, *66*, 2021–2029. [[CrossRef](#)]
41. Takeuchi, A.; Inoue, A. Classification of bulk metallic glasses by atomic size difference, heat of mixing and period of constituent elements and its application to characterization of the main alloying element. *Mater. Trans.* **2005**, *46*, 2817–2829. [[CrossRef](#)]
42. Cullity, B.D. Elements of X-Ray diffraction. *Am. J. Phys.* **1957**, *25*, 394–395. [[CrossRef](#)]